Volume 2
Number 11
November 2020
Pages 4971–5480

Nanoscale Advances

rsc.li/nanoscale-advances

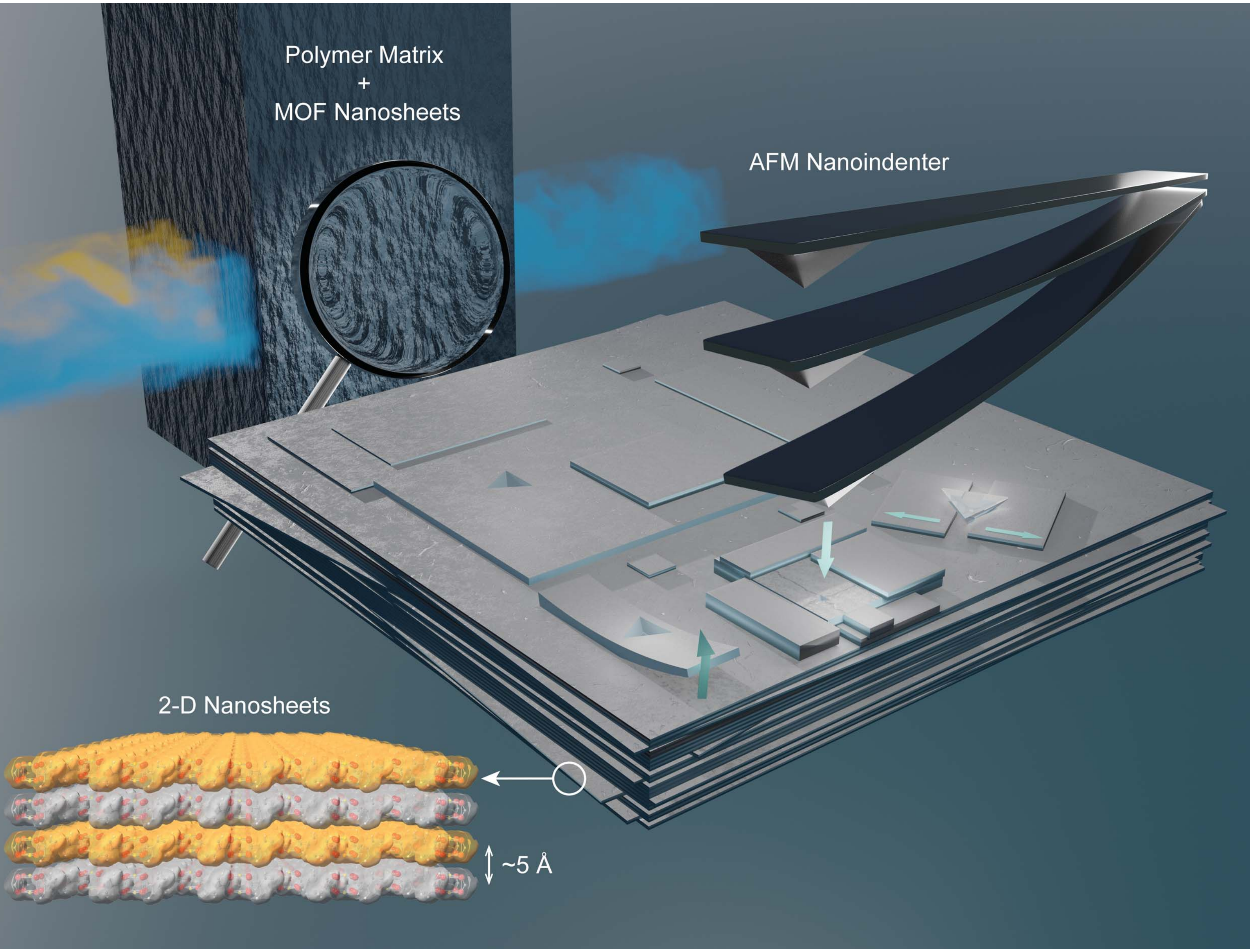

ISSN 2516-0230

ROYAL SOCIETY OF CHEMISTRY

PAPER
Jin-Chong Tan *et al.*
Nanomechanical behavior and interfacial deformation beyond the elastic limit in 2D metal–organic framework nanosheets

NCNST

Nanoscale
Advances

ROYAL SOCIETY
OF CHEMISTRY

PAPER

View Article Online
View Journal | View Issue

Check for updates

Cite this: *Nanoscale Adv.*, 2020, **2**, 5181

Nanomechanical behavior and interfacial deformation beyond the elastic limit in 2D metal–organic framework nanosheets†

Zhixin Zeng,[a] Irina S. Flyagina[ab] and Jin-Chong Tan[*a]

Nanoscale mechanical property measurements of nanoporous nanosheets face many challenges. Herein we show atomic force microscope (AFM)-based nanoindentation to probe the nanoscale mechanical properties of a 2-D metal–organic framework (MOF) nanosheet material containing atomic-sized pores, termed CuBDC [copper 1,4-benzenedicarboxylate]. The sample thickness ranged from ~10 nm (tens of monolayers) up to ~400 nm (a stack of multilayers). In terms of its elastic–plastic properties, the Young's modulus ($E \sim 23$ GPa) and yield strength ($\sigma_y \sim 450$ MPa) were determined in the through-thickness direction. Moreover, we characterized the failure mechanisms of the CuBDC nanosheets, where three failure mechanisms were identified: interfacial slippage, fracture of the framework, and delamination of multilayered nanosheets. Threshold forces and indentation depths corresponding to these failure modes were determined. To gain insights into the failure mechanisms, we employ finite-element models with cohesive elements to simulate the interfacial debonding of a stack of 2-D nanosheets during the indentation process. The nanomechanical AFM methodology elucidated here will pave the way for the study of other 2-D hybrid nanosheets and layered *van der Waals* solids.

Received 12th June 2020
Accepted 11th August 2020

DOI: 10.1039/d0na00475h

rsc.li/nanoscale-advances

1. Introduction

Because the underlying structure of crystalline nanomaterials controls their functions, understanding the fundamental structure–property relations is important to enable practical applications of new materials.[1–4] Amongst the vast family of two-dimensional (2-D) nanomaterials, we will focus on metal–organic framework (MOF) nanosheets which show benefits in several potential applications. For example, novel devices constructed from 2-D nanosheets show good tunability and efficacy in capacitance,[5,6] energy conversion,[7] electrocatalysis,[8] luminescence,[9] and gas separation.[10] While there are predictions of certain mechanical properties of 2-D structures at the nanoscale using theoretical techniques such as density functional theory[11,12] and molecular dynamics,[13–16] hitherto, to the best of our knowledge there is not yet any rigorous experimental study for quantifying the nanoscale mechanical behavior and interfacial effects of nanoporous MOF nanosheets (with atomic-sized pores) in the elastic–plastic regime. Lack of systematically characterized experimental data of mechanical properties is one of the limiting factors that hinders confident evaluation of the practicability of 2-D MOF nanosheets. The mechanical characterization of nanosheets *via* an experimental approach is challenging owing to the mutual interplay between the adjacent nanosheets (*viz.* interlayer interactions),[17] compounded by several major obstacles, such as the difficulties of small sample preparation, precise implementation of the fine-scale force and displacement measuring techniques, and the accurate interpretation of material structural failure data.

A number of mechanical characterization experiments on 2-D nanosheets have been reported to date, where depth-sensing indentation has been widely used.[18–21] This includes the use of atomic force microscope (AFM)-based nanoindentation and the instrumented nanoindentation techniques.[22] Thus far, studies have concentrated on either the ultra-stiff nanosheets, graphene (Young's modulus, $E \sim 1$ TPa)[20,23–25] and boron nitride ($E \sim 250$ GPa) in particular,[17,26] or the very soft biological samples such as protein nanosheets.[27] Although there are a few experiments performed on nanosheets with stiffness lying in the range of a few gigapascals to tens of gigapascals, such as the dense 2-D hybrid framework of Mn 2,2-dimethylsuccinate nanosheets ($E = 9.4$–20.9 GPa depending on crystal orientation due to anisotropy)[28] and the bismuth telluride nanosheets ($E = 11.7$–25.7 GPa),[29] very few studies have systematically explored

---

[a] *Multifunctional Materials & Composites (MMC) Laboratory, Department of Engineering Science, University of Oxford, Parks Road, Oxford, OX1 3PJ, UK. E-mail: jin-chong.tan@eng.ox.ac.uk*

[b] *Frumkin Institute of Physical Chemistry and Electrochemistry Russian Academy of Sciences, 31, bld.4, Leninsky prospect, Moscow, 119071, Russia*

† Electronic supplementary information (ESI) available: Synthesis method, characterization of the geometry of the cube-corner indenter tip, AFM topology of the nanosheets and the residual indents, the ratio of the pile-up height to the indentation depth, the iterative method for determining plasticity, finite element models, the influence of the varying Poisson's ratios on the quantification of the Young's modulus, and the threshold forces and depths resulting in the different failure modes. See DOI: 10.1039/d0na00475h

the mechanical behavior of nanoporous MOF nanosheets. There are recent examples using standard instrumented nanoindentation techniques to characterize the out-of-plane mechanical behavior of 2-D organic–inorganic perovskites, where $E = 6$–12 GPa has been reported for dense hybrid frameworks incorporating different organic spacer molecules.[30] There is a report on the AFM nanoindentation of large flakes of $[\mathrm{Cu}(\mu\text{-pym}_2\mathrm{S}_2)(\mu\text{-Cl})]_n$ MOF nanosheets, where the 2-D samples were suspended over a holey SiO_2 substrate and probed by using an AFM tip in the bending mode to estimate the Young's modulus and rupture stress.[31]

In this work, we demonstrate a direct AFM-based nanoindentation approach (unlike the foregoing AFM bending method)[20,31] to perform a quantitative study of the nanoscale mechanics of nanoporous 2-D MOF nanosheets containing atomic-sized pores. Using a combination of indentation measurements and finite-element modeling, we determined not only the elastic–plastic properties, but also gained a deeper understanding of the specific deformation mechanisms responsible for the structural failure of 2-D nanosheets. It is envisaged that the methodology and analysis exemplified in this study will be applicable for the characterization of a vast range of topical 2-D *van der Waals* materials in the field.[32]

Copper 1,4-benzenedicarboxylate (CuBDC) nanosheets, an example of MOF nanosheets, were selected as the model material to develop the AFM nanoindentation technique for quantifying the nanoscale mechanical properties of 2-D MOF structures. CuBDC is composed of square-planar copper(II) dimers coordinated to the BDC linkers.[33] CuBDC crystallizes in the monoclinic $C2/m$ space group, where its adjacent nanosheets form a nanoporous layered architecture as depicted Fig. 1.

The CuBDC nanosheets form thin 2-D crystals with a rectangular morphology as shown in Fig. 2. The constituent CuBDC layers are stacked along the $[\bar{2}01]$ crystal axis and held together by *van der Waals* forces, yielding a periodic framework structure (Fig. 1a). From the AFM topographic images, it can be seen that the thickness of the CuBDC nanosheets ranges from ~10 nm (*viz.* the thinnest nanosheet consists of ~19 monolayers as shown in Fig. 2c) to 400 nm (comprising hundreds of monolayers). Exfoliation of thin nanosheets out of the thicker multilayered stacks is important for a number of reasons; for example, thin nanosheets offer a source of building blocks for constructing 2-D thin-film devices and flexible electronics.[7,34] Another example application lies in composite mixed-matrix membranes, by incorporating exfoliated nanosheets of CuBDC in a polymer matrix to enhance the gas separation performance for a mixture of CO_2 and CH_4.[10]

On account of the weak *van der Waals* forces, there is a risk of delamination and other forms of interfacial failure caused by the sliding of nanosheets during shear deformation. Therefore, design and fabrication of functional devices integrating nanosheets will require an improved understanding of not only the common mechanical properties such as the elastic moduli but also a better understanding of interfacial failure modes, because the sliding and rupture of nanosheets could affect the function of the devices. Furthermore, the interfacial failure between the nanosheets will impede accurate measurement of the depth-sensing indentation technique, resulting in

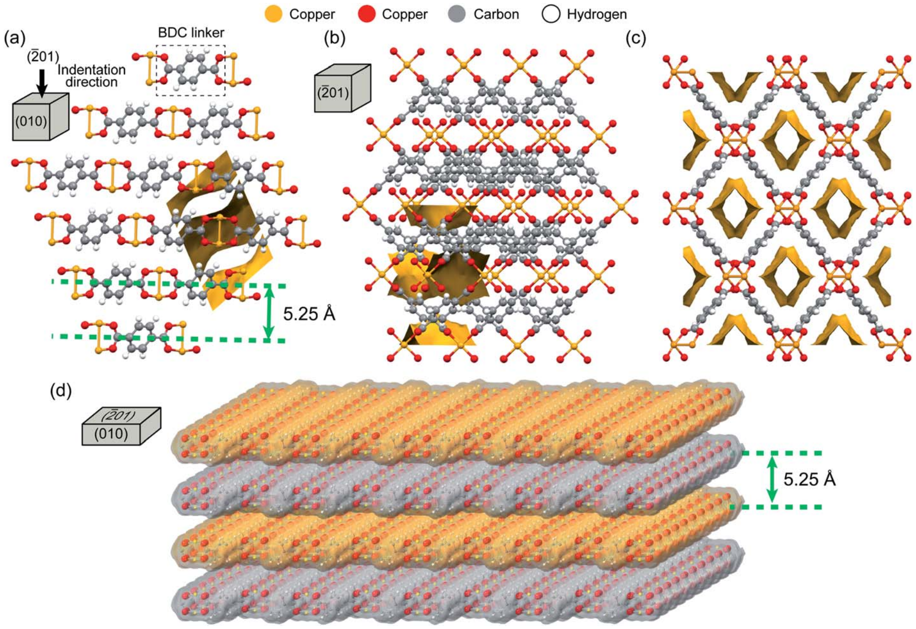

Fig. 1 2-D crystalline structure of the CuBDC layered framework. The diatomic copper atoms are coordinated to the BDC linkers to form the copper paddle wheels. Pore channels are designated as yellow surfaces, corresponding to the solvent accessible volume using a probe size of 1.2 Å. (a) View down the [010] crystal axis, showing the stacking direction of the 2-D layers (monolayer thickness ~0.5 nm), in which the AFM nanoindenter penetrates along the $[\bar{2}01]$ crystal axis (*i.e.* downward arrow). (b) View down the $[\bar{2}01]$ axis. (c) View down the pore channels oriented along the [001] crystal axis. (d) 3-D view depicting the 2-D layered architecture of CuBDC comprising a stack of four monolayers. Oxygen, hydrogen and carbon atoms are shown in red, white, and grey, respectively.

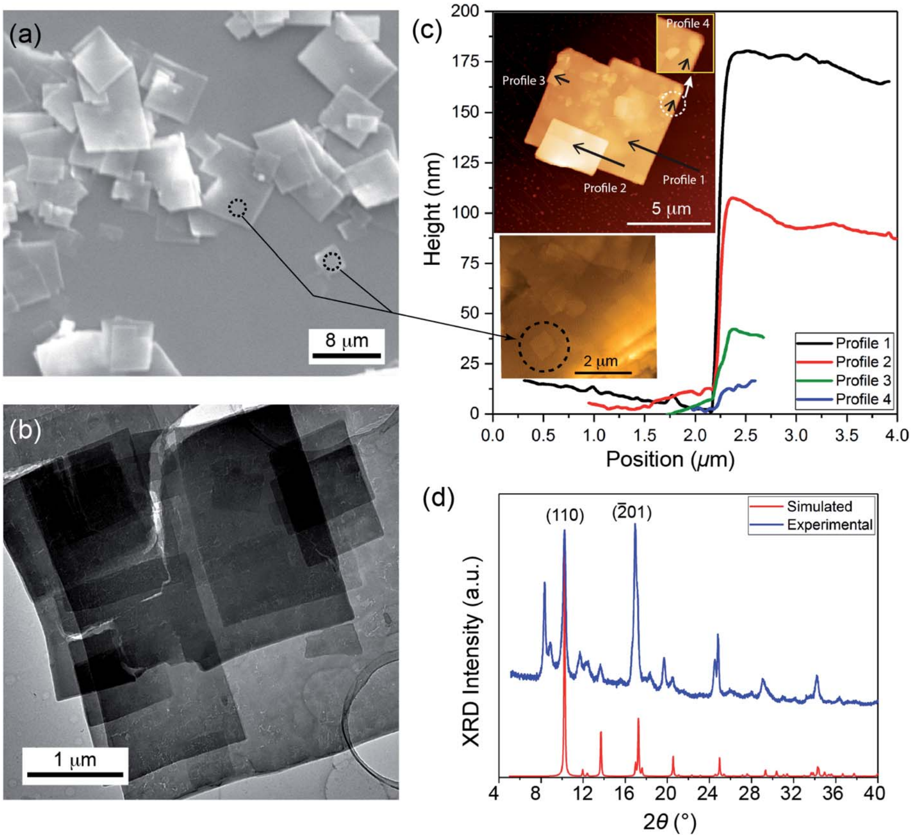

Fig. 2 Characterization of the CuBDC nanosheets. (a) Scanning electron microscope (SEM) image; (b) transmission electron microscope (TEM) image; (c) AFM height topography of the multilayered CuBDC nanosheets, revealing the surface features of the nanosheet stacks (inset) not visible under the SEM; (d) experimental and simulated[10] X-ray diffraction (XRD) patterns. Note that the extra peaks, for example at $2\theta = 8.3°$, 8.9°, and 19.6° are due to the thermal desolvation of the framework which is reversible upon the addition of solvent molecules; for further details see ref. 35.

distortion of the indenter load-penetration depth (*P*–*h*) data or an erroneous indenter-to-sample contact area. In this study, we address these challenges to enable quantitative determination of the intrinsic 2-D mechanical behavior.

2. Experimental section

2.1. Synthesis and characterization of CuBDC nanosheets

The CuBDC nanosheets were synthesized using the layering technique reported by Rodenas *et al.*[10] The synthesis steps are described in the ESI S1.† The morphology of the nanosheets was examined using a Carl Zeiss Evo LS15 VP scanning electron microscope (Fig. 2a), a JEM-2100 LaB6 transmission electron microscope (Fig. 2b), and a Veeco Dimension 3100 atomic force microscope equipped with a Tap300Al-G probe operating in the tapping mode (Fig. 2c). The crystal structure of the CuBDC nanosheets was confirmed by powder X-ray diffraction (XRD) using a Rigaku Miniflex diffractometer (Fig. 2d).

2.2. AFM nanoindentation using a diamond-tipped cantilever probe

The AFM nanoindentation measurements were performed using a Veeco Dimension 3100 instrument operating in the indentation mode, equipped with a Bruker PDNISP probe (a cube-corner diamond tip, see Fig. S1 in the ESI†). The probe has a 350 μm long cantilever made of stainless steel, where a cube-corner diamond indenter tip is mounted at the end of the cantilever. The spring constant and contact sensitivity of the probe were calibrated, and given as 152.285 N m^{-1} and 256.6 nm per volt, respectively. The high sensitivity of the AFM instrument facilitates the precise detection of the initial contact point between the indenter and the nanosheets. One of the main advantages of AFM is the ability to control and detect small indentation load (force sensitivity <0.05 nN) and to apply a shallow indentation (displacement sensitivity $\lesssim$0.05 nm).[36] Here, we applied the criterion for identifying the contact point as and when the contact stiffness, $dP/dh \geq 25$ N m^{-1}, was reached. Further details on sample preparation are given in the ESI.†

2.3. AFM nanoindentation methodology and analysis of *P*–*h* data

2.3.1. Oliver and Pharr method. Each AFM nanoindentation experiment generated a force-displacement (*P*–*h*) curve, which was analyzed using the Oliver and Pharr (OP) method to determine the Young's modulus (*E*) of the CuBDC

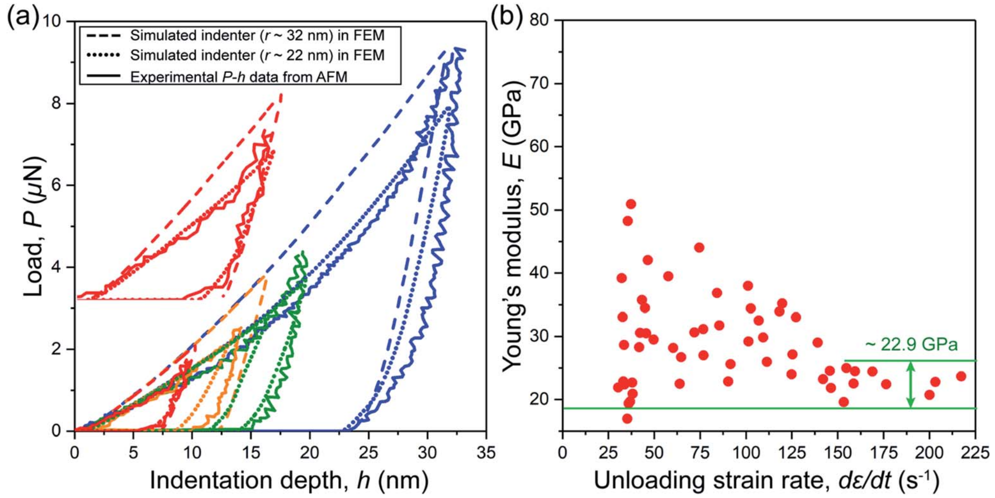

Fig. 3 (a) Representative indentation load *versus* surface penetration depth (P–h) curves measured by AFM nanoindentation experiments (solid lines) and modeled by the finite-element (FE) method (dashed and dotted lines for indentation using the two simulated indenter tips with a tip radius of 32 nm and 22 nm, respectively). Both the elastic and plastic deformation behavior predicted by the FE models resemble the experimental data. (b) Young's modulus (E) of the CuBDC nanosheets determined using the Oliver & Pharr method, plotted as a function of the unloading strain rate of the nanoindenter tip.

nanosheets.[37] Every data point of E in Fig. 3b was obtained from an individual loading-unloading indentation cycle.

2.3.2. Unloading strain rate method. Indentation of materials that are either porous or brittle and either viscoelastic or defective, usually exhibits failures or creep, which can introduce significant distortions in the P–h curves. It was found that at the unloading stage, the additional displacement along the indentation direction still dominates the overall movement, overwhelming the elastic recovery in the opposite (*viz.* unloading) direction.[22] Consequently, the incipient segment of the unloading curve no longer reflects the intrinsic elastic property. To overcome this limitation, an augmented unloading strain rate method[22] was implemented first to retrieve a valid P–h curve that reflects the true elastic–plastic response of the nanosheets. Subsequently, we employed the Oliver and Pharr method[37] to extract the slope of the unloading curve ($\mathrm{d}P/\mathrm{d}h$) required for the calculation of the Young's modulus. We found that this combined approach is effective for very shallow AFM-based nanoindentation of framework materials with nanoscale porosity.

2.3.3. Iterative method for determining plasticity. In the finite-element (FE) model, the elastic–plastic material properties were defined as listed in Table S3 (ESI†). For elasticity, the Young's modulus can be measured using AFM nanoindentation (Fig. 3). We developed an iterative method to determine the plastic properties, which was assumed to follow a power-law relation between the stress (σ) and plastic strain (ε_p),[38] and it can be described by the Hollomon's equation:[39]

$$\sigma = k\varepsilon_\mathrm{p}^n \tag{1}$$

The work-hardening exponent n exerts an influence on the height of the pile-ups of the CuBDC nanosheets.[37] In detail, the hardening of the material near the indenter restrains the rising flow towards the surface of the sample and this can be associated with the collapse of MOF nanopores, leading to densification of the open framework. At the end of the elastic regime of a stress–strain curve, the strength coefficient (k) can also be defined based on the elastic modulus:

$$k = \frac{\sigma_y}{(\varepsilon)^n} = \frac{\sigma_y}{\left(\dfrac{\sigma_y}{E}\right)^n} \tag{2}$$

at first, it was assumed that the strength coefficient of CuBDC is relatively high ($k \gtrapprox 150$), meanwhile, the work-hardening exponent (n) is in the range of 0.1 to 0.3 (these assumptions were later verified because $n \sim 0.17275$ and $k \sim 863.52053$ were obtained using the iterative method).

According to the empirical relation proposed by Matthews,[40] the ratio between the height of residual pile-up, s, after the withdrawal of the indenter tip and the indentation depth at the maximum load, h (see Fig. 4c), is assigned based on the work-hardening exponent (n):

$$\frac{s}{h} = \frac{1}{2}\left(\frac{2+n}{2}\right)^{2(1-n)/n} - 1 \tag{3}$$

The value of s was measured from the AFM images of the indents (Fig. 4a–c). The study of 32 indents gave us the arithmetic mean value of $s/h \sim 0.10551$ (see Table S2 in the ESI†). By substituting the value into eqn (3), we obtained $n = 0.17275$.

The iterative method is conditioned upon acquisition of the work-hardening exponent, which is the fixed part in Fig. 4d. Initially, an estimated value of the yield stress (σ_y) was assigned to eqn (2), yielding a starting value of k. Subsequently, by substituting the values of k and n into eqn (1), the first predicted plasticity parameter of the CuBDC nanosheets was produced. Inputting the Young's modulus ($E = 22.9$ GPa) and the plastic

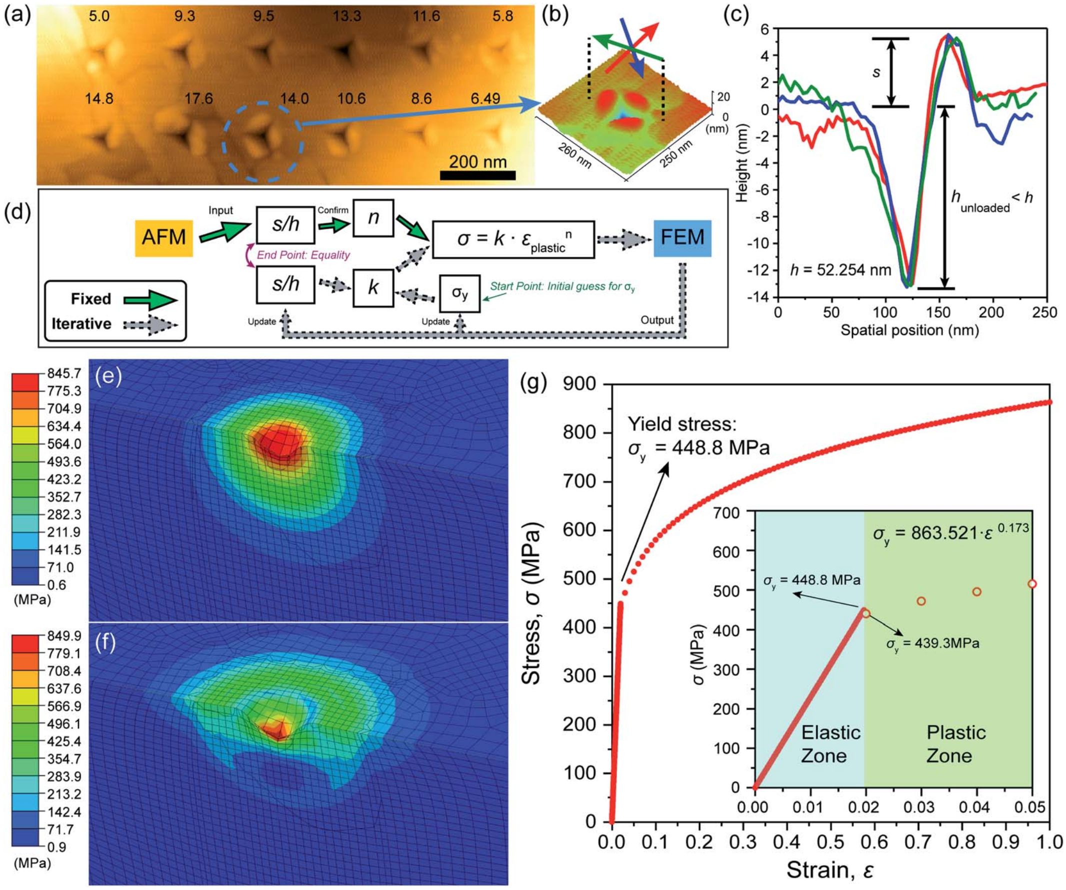

Fig. 4 (a) AFM height images of the residual indents on a stack of CuBDC nanosheets, where the pile-ups generated by using the cube-corner indenter are clearly visible. The residual indentation depth (in nm) is marked above each indent. (b) Height profiles shown as a 3-D depth color map, where the sectional profiles marked by the three arrows are plotted in (c). (d) Procedure of the iterative method. (e and f) Finite-element (FE) model showing the Mises stress contour of the simulated indentation employing a contact-area equivalent conical tip (details in Table S1†): (e) indentation during the loading stage, and (f) the FE model at the fully unloaded stage (the indenter is not shown for clarity). (g) Stress–strain curve showing the elastic–plastic transition behavior of the CuBDC nanosheets around the yield point σ_y, derived from the converged outcome of the iterative method (d).

property into the FE model, we obtained new values of s/h and σ_y. Through the iterative process, the convergence criterion was met when the updated values of $\sigma_y = 448.8$ MPa (Fig. 4g) and $k = 863.52053$ were used as inputs in the FE model, which returned the s/h ratio that matched the one measured in the AFM nanoindentation experiment, *viz.* $s/h \sim 0.10551$.

2.3.4. Finite-element (FE) modeling. The FE method was implemented in the ABAQUS CAE program to simulate the indenter-to-sample contact, the non-linear structural deformations, and the patterns of distortions (Fig. 5) caused by failures of the CuBDC nanosheets. A continuum slab model representing the CuBDC nanosheets was meshed using the 8-node linear brick elements with reduced integration and hourglass control (*C3D8R*). We employed the ABAQUS/Explicit solver which is tailored for calculating complex contact mechanics problems. It is noted that the oscillation of the *P*–*h* curves reported in the literature[41,42] was overcome by applying a refined mesh in this study, and the mesh convergence was achieved as shown in the ESI (Fig. S8†). The indenter in the FE model is a discrete rigid cone with an equivalent inclusive angle as the real indenter, in which a curved apex with a radius of $r \sim 22$ nm (see Fig. S1 in the ESI†) was created to prevent excessive mesh distortion.

In the FE models where the nanosheet interfacial failures were defined, the interaction between the adjacent nanosheets was modelled using the cohesive elements whose damage under stress is initiated in accordance with the maximum nominal stress criterion (ESI S6†). Moreover, we implemented the Johnson–Cook fracture criterion[43] to model the failure of the nanosheets allowing the strain rate effects to be studied (ESI S7†). The Johnson–Cook model was initially proposed for metals, but has also been applied to softer materials like polymers.[44]

3. Nanoscale mechanical properties of CuBDC nanosheets

3.1. Quantification of through-thickness elasticity

Fig. 3a shows the representative load-displacement (*P*–*h*) curves obtained from the AFM nanoindentation measurements for a series of experiments where the maximum surface penetration

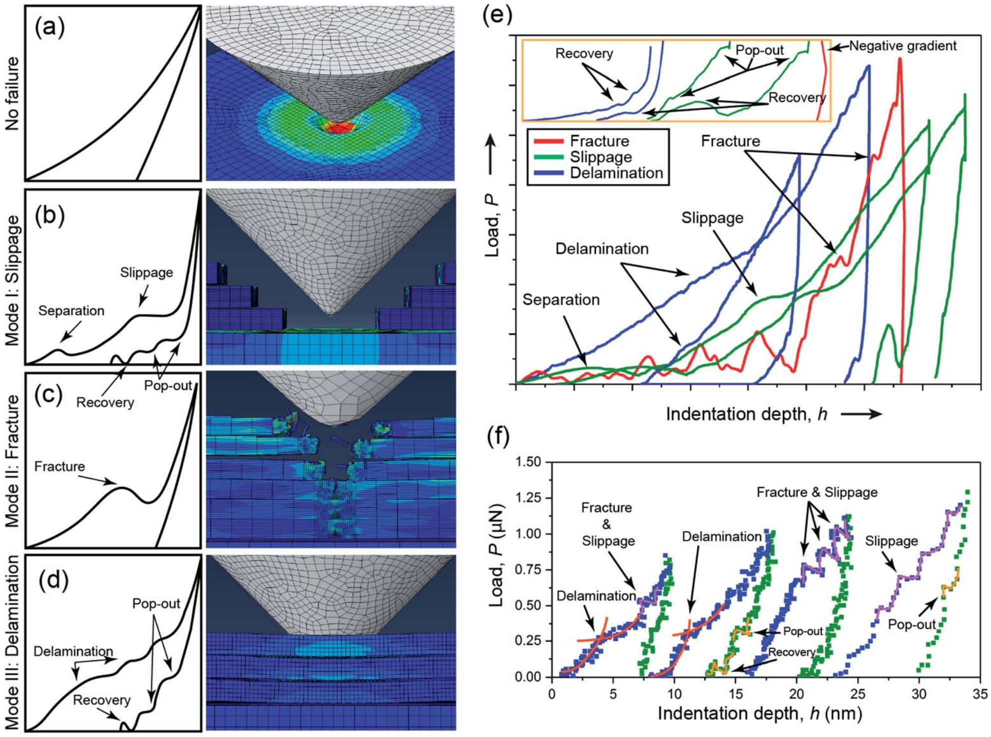

Fig. 5 (a–d) Schematics illustrating the possible distortions of the P–h curves due to the different nanosheet failure modes, the corresponding FE models are shown in the right panels. For comparison, panel (a) depicts the AFM nanoindentation of an ideal nanosheet stack (*viz.* perfectly bonded multilayers) without any material failure. (e) The FE models capture the main characteristics observed in the experimental P–h curves in (f) measured by AFM nanoindentation. The inset in (e) shows a magnified view of the unloading curves from FE modeling.

depth was varied from about 10 nm to 32 nm. Instead of indenting directly onto a thin stack of CuBDC nanosheets, on which the substrate effect on the elasticity measurement is prone to arise, we performed the AFM nanoindentation experiments on the nanosheet stacks of sufficient thickness to satisfy the 10% indentation depth rule in order to minimize the influence of the substrate. Fig. 3b presents the Young's modulus (E) values of the nanosheets derived from a total of 56 nanoindentation experiments. It can be seen that the through-thickness stiffness of the CuBDC nanosheets measured by a low unloading strain rate is highly scattered and overestimated (up to $E \sim 52$ GPa). This is likely due to time-dependent deformations, such as creep deformation that exaggerates the stiffness value. Therefore, an augmented unloading strain rate method[22] was implemented, with which we found the Young's modulus starts to converge with an increasing unloading strain rate.

When the unloading strain rate surpasses $\sim 140\ \mathrm{s}^{-1}$, it was found that the through-thickness stiffness value converged to an arithmetic mean of $E = 22.9$ GPa (Fig. 3b). The Poisson's ratio of CuBDC was taken as $\nu = 0.4$; its effect on the Young's modulus of the CuBDC nanosheets is given in the ESI (see Fig. S11†). The dashed and dotted curves in Fig. 3a are the resulting P–h curves predicted by the FE model by assuming an ideal material (without any material failure). The material properties defined in the model match the elastic constants determined from the AFM nanoindentation experiments and the plasticity parameters obtained from the iterative method (see the section below).

3.2. Quantification of plastic deformation: analysis using an iterative method

Plastic deformation is an important factor to be considered in indentation experiments and it can be characterized in relation to the height of the residual indentation pile-up (Fig. 4a–c). Systematic analysis of indentation pile-ups of (monolithic) elastic–plastic solids has been reported by Taljat and Pharr.[45] In this study, we employed FE modeling (Fig. 4e and f) in combination with the iterative method to establish the plastic deformation behavior of the CuBDC nanosheets, on the basis of the correlation between the plasticity and the height of the pile-ups formed in the periphery of the indents. The flow chart in Fig. 4d summarizes the procedures of the iterative method we proposed, in which the results obtained from both the AFM-based nanoindentation experiments and the FE modeling were utilized to establish the value of the yield stress, σ_y (see the Experimental section).

As shown in Fig. 4g, we found the yield stress of the CuBDC nanosheets to lie in the range of $\sigma_y = 439$–449 MPa, bridging the elastic and plastic zones. Herein we propose that the yield phenomenon is linked to the plastic flow of the 2-D layered architecture prevalent in the CuBDC nanosheets, as evidenced by the large pile-ups observed in the vicinity of the residual indents, see Fig. 4b and c. Nonetheless, hardness of a layered 2-D structure measured by the AFM-based nanoindentation is significantly influenced by the sliding movement of the interlayers (*viz.* the sliding tendency),[17] where the indentation depth can no longer indicate the true resistance of the nanosheets against plastic deformation (Fig. S12 in the ESI†).

4. Identification of failure mechanisms

4.1. Nanoscale 2-D failures causing distortions of the indentation curves

In this section, we employed AFM-based nanoindentation to characterize the mechanical failures of the CuBDC nanosheets. Fig. 5 shows the distortions of the *P*–*h* curves because of nanosheet failures induced by indentation. We propose three distinctive deformation modes underpinning the failure of the CuBDC nanosheets: Mode I – interfacial slippage between nanosheets, Mode II – fracture of nanosheets, and Mode III – interfacial delamination of nanosheets.

In Mode I, the coplanar nanosheets are separated by the penetrating indenter that causes the nanosheets to slide sideways under shear deformation. Layer separation occurs because the coplanar nanosheets are weakly bound by *van der Waals* interactions. Typically, sliding of the nanosheets produces a stepwise distortion in the measured *P*–*h* curves, which resembles the "pop-in" phenomenon observed in other 2-D materials.[28] During the slippage failure, a force analysis was conducted (Fig. 6a) to shed light on the underlying mechanism. For Mode II, we found that the fracture of the CuBDC framework was due to stress concentration generated by using the indenter, and the phenomenon can be identified as the "humps" in the *P*–*h* curves. A similar failure mode has been reported in the two-layer stacked graphene indented by AFM[23] and the boron nitride nanosheets studied by *in situ* indentation.[46] In the case of Mode III, bending of a stack of nanosheets can lead to interlayer delamination failure during the loading stage, ascribed to the bending moment from the peripheral regions of the indent. In other words, the stretching of the cohesive layer normal to the nanosheet plane eventually led to the breakage of the adjacent nanosheets (see Fig. 6b). In addition, the "pop-out" and recovery phenomena at the unloading stage were also observed and their mechanisms will be discussed in the next section.

4.2. Force analysis of the failure modes

Fig. 6a and b illustrate the origin of the distortions in the *P*–*h* curves, which occur due to the interfacial slippage and

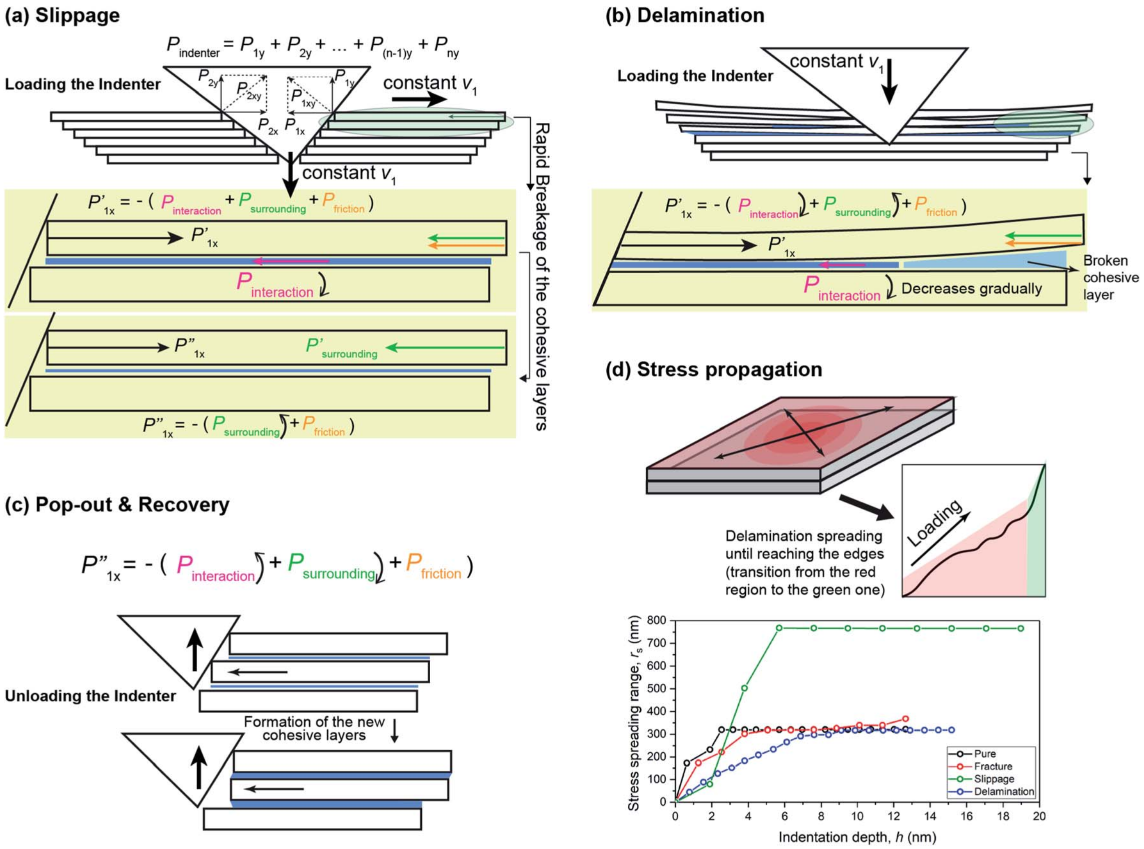

Fig. 6 Schematic illustration of the evolution of the resolved forces between the indenter and a stack of nanosheets, as well as between adjacent nanosheets under different failure modes: (a) the interfacial slippage at loading due to shear, (b) the delamination at loading due to bending, and (c) the mechanism of the pop-out and recovery phenomenon at unloading. Note that in the enlarged views, the *van der Waals* interactions between the nanosheets are modeled by the cohesive layers in the FE model (in blue, highlighted in a yellow background). (d) Stress propagation mechanism: (top) in terms of the nanosheet delamination, the diagram depicts the effect of the plane stress propagation on the *P*–*h* curve; (bottom) the plane stress spreading range with an increasing depth predicted by the FE model using the equivalent conical indenter.

delamination of the nanosheets, respectively. Regarding the slippage mode, the indenter initially overcomes the interfacial forces that bind the nanosheets together (preventing separation of the nanosheets). The breakage of this interfacial constraint is indicated by the first broad hump shown in the schematic P–h curve (Fig. 5b). Subsequently, the indenter starts to push the nanosheets sideways apart, while the cohesive layers deform under the shear forces until the complete failure occurs. During this process, the resolved indention forces (P'_{ix}, $i = 1, 2, 3,\ldots, n$ layers) which are horizontally exerted between the indenter and the nanosheets gradually decrease due to the growing detachment of the cohesive layers. Therefore, the interaction force between the adjacent nanosheets ($P_{\text{interaction}}$) decreases gradually until the cohesive layer is fully damaged. This results in the pop-in segment of the P–h curve, corresponding to the slippage shown on the P–h curve (Fig. 5b). By contrast, the breakage of the cohesive layers progresses relatively slower in the delamination mode than in the slippage mode (see Fig. 6d), because the bending stress that leads to delamination propagates slower than the acting shear stress while the nanosheets slide relative to one another. Therefore, the gradient of the distorted loading curve in the delamination mode is declining at a lower rate compared with the more abrupt stepwise pop-in deformation detected in the slippage mode.

We also observed a pop-out phenomenon while withdrawing the indenter. This suggests the formation of a new cohesive layer *via* restoration of the broken *van der Waals* interactions between the nanosheets. The resolved counter-acting forces from the indenter (P'_{nx}) are equivalent to the sum of the forces provided by the new cohesive layers ($P_{\text{interaction}}$), the restraining forces exerted by the surrounding materials ($P_{\text{surrounding}}$), and the friction force (P_{friction}). In fact, the friction also changes with the penetration of the indenter as a result of the varying normal force, and it can also affect the resultant P–h curves.[47] The model in Fig. 6c shows that the interaction force exerted by the new cohesive layer increases while the force exerted by the surrounding material decreases during unloading of the indenter. Thus, the interplay between the indenter and the nanosheets in a quasi-equilibrium state culminates in the pop-out deformation observed in the unloading curves. Interestingly, a force recovery process was witnessed in the experiment emerging right before the indenter-to-sample interaction was reduced to zero (Fig. 5f). The reason of the recovery is similar to the pop-out phenomenon, but instead of reaching the force equilibrium, the augmentation of $P_{\text{interaction}}$ was overwhelming compared with the reduction of $P_{\text{surrounding}}$. Therefore, the unloading P–h curve shows a rise in the resultant force (Fig. 5d). The force recovery in the P–h curve can be seen near the end of the indenter withdrawal when $P_{\text{surrounding}}$ is close to being fully relaxed. In the FE model, both the pop-out and recovery phenomena were simulated as shown in Fig. 5e.

Additional indentation cycles were performed on two thin CuBDC nanosheet stacks (thickness, $t \sim 16$ nm and $\sim$48 nm) placed on a glass substrate in order to investigate plasticity on the upper surface of the nanosheets when the substrate took effect. No visible radial cracks were observed at the residual indents (Fig. S4†), which suggests the relatively resilient nature of the surrounding CuBDC framework. In other words, the constraint imposed by the surrounding CuBDC framework has an impact (*i.e.* $P_{\text{surrounding}}$) on the indentation area, which is consistent with the force analysis in Fig. 6. In contrast to our findings, indentation experiments using a sharp indenter tip (*e.g.* cube-corner) on thin but stiffer layers such as the silicon ($t \sim 50$ nm)[48] and the hybrid YAS-GNP coatings ($t = 169 \pm 10$ μm) on a silicon carbide substrate[49] were reported to generate dramatic radial cracks.

The P–h curves from AFM nanoindentation may show large-scale distortions as shown in Fig. 5d. By characterizing such distortions, the threshold forces responsible for the failures of CuBDC nanosheets at the nanoscale can be quantified (Fig. S13†). We estimated the threshold conditions that trigger the failure modes I, II, and III of the CuBDC monolayer as summarized in Table 1; the evolution with indentation depth also was characterized (Fig. S14†). Fig. 6d shows that when the indentation depth is below $\sim$2 nm, the stress spreading area of the slippage mode is less than the ones for delamination and fracture modes. However, when the indentation depth exceeds $\sim$2 nm and $\sim$2.5 nm, the stress area for slippage surpasses the areas for delamination and fracture, respectively. Likewise, we found that the threshold forces of the three modes in Table 1 are ranked in the same order (slippage < delamination < fracture). Accordingly, the stresses required for delamination were found to be $\sim$1.8 times and $\sim$5.5 times greater than the ones needed to induce slippage and fracture, respectively.

4.3. Small-scale continuous failures during AFM nanoindentation

In Fig. 7a, the P–h curve in black obtained from AFM nanoindentation typifies the response of the CuBDC nanosheet without experiencing material failure, while the other three

Table 1 Threshold values of the indentation force, depth, projected area of indent, area of the stress field acquired based on Fig. 6d (assuming it is a circular stress field propagating normal to the indentation direction), and stress (force/area of the stress field) leading to the three distinctive failure modes of a monolayer of the CuBDC nanosheet

	Threshold values				
Failure modes	Force (nN)	Depth (Å)	Projected area of indent (nm^2)	Area of stress field (nm^2)	Stress (MPa)
I. Slippage	42.6	6.5	1.1	$\sim$2290	9.3
II. Fracture	70.4	6.4	1.1	$\sim$23 779	3.0
III. Delamination	56.0	5.8	0.9	$\sim$3421	16.4

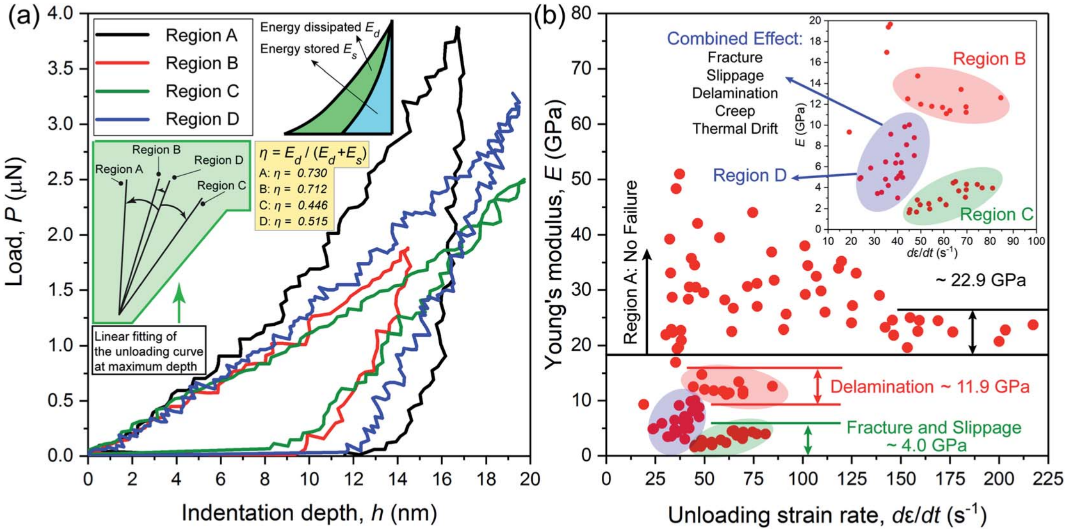

Fig. 7 (a) Representative P–h curves from AFM nanoindentation of the CuBDC nanosheets showing indentations that cause: no failure (curve in black: region A), the delamination of nanosheets (curve in red: region B), a coupled effect of the fracture and slippage of the CuBDC nanosheets (curve in green: region C), and a combination of all possible time-dependent responses such as creep, thermal drift, and the abovementioned failure modes (curve in blue: region D). Linear fittings of the incipient unloading curves are shown in the green panel in the inset. The energy dissipation fraction (η) is given in the yellow panel in the inset. (b)The Young's modulus determined using the Oliver and Pharr method from the unloading curves of the four types of the P–h curves in (a), showing a significant loss of stiffness in regions B, C, and D *versus* region A.

representative P–h curves show distinct responses when indentation stress induces failure. Such a difference was exemplified in the scatter of the stiffness values in Fig. 7b depicting the four distribution regions, into which the data points fall. Only region A describes the intrinsic mechanical property of CuBDC owing to the absence of significant stress-induced framework failure and other time-dependent deformations (*e.g.* creep and thermal drift). Otherwise, the CuBDC framework could experience a varying degree of stiffness loss and reduced hardness (designated as regions B, C, and D) depending on the type of the failure mode. In addition, the energy loss (see Fig. 7a) of the indentations represented by the regions B, C, and D was observed to be lower than in region A. The results suggest that in the scenarios described by regions B, C, and D, part of the deformation was contributed by other forms of mechanical behavior (*e.g.* fracture, sliding, and delamination) dissipating less energy than the plastic deformation determined in region A.

It is worth noting that the Young's moduli in regions B, C, and D in Fig. 7b were derived from the P–h curves that exhibit no abrupt distortions over the history of the entire P–h curve. The stiffness data thus suggest that the occurrence of failures is a continuous process, compared to the characteristic failure modes evidenced in Fig. 5d. The data points in region B might correspond to delamination of the CuBDC nanosheets (Mode III) induced by the AFM indenter. This inference is based on the observation that delamination causes less additional indentation displacement than the other two failure modes, and therefore, it brings about less stiffness loss. Conversely, the indentation tests that returned the data points in region C may be attributed to the coupled effect of interfacial sliding/slippage (Mode I) and fracture (Mode II) of the nanosheets that produced a higher level of stiffness loss. The interfacial sliding in this study mainly refers to the horizontal sliding of nanosheets normal to the indenter axis, although the sliding along the indentation direction may also cause stiffness loss, such as that reported in ref. 50.

Regions B and C are the steady states subsequent to region D with an increasing unloading strain rate. Akin to the effect of surpassing the time-dependent behavior such as creep and thermal drift in the indention direction, a sufficiently high unloading strain rate reduces the deformation of the nanosheets in the horizontal direction along, P'_{nx} and thus contributes to the convergence of the Young's modulus from region D to C. With this in mind, the unloading strain rate principle[22] can also be extended to suppress failure since high loading-unloading strain rates shorten the time available for crack propagation. Fig. 7b also shows that the indentations in region D were implemented at a relatively lower unloading strain rate, therefore additional indentation displacements were accumulated by a combination of factors: fracture, sliding, delamination, creep, and thermal drift. In this case, the unwanted effects of time-dependent processes in region D could be mitigated by raising the unloading strain rate of the indenter.

5. Conclusions

In this work, a quantitative approach is demonstrated for using the AFM-based nanoindentation technique to study the mechanical properties of the CuBDC nanosheets. The main results are summarized as follows:

- A quantitative study of the nanoscale mechanics of 2-D nanosheets is challenging especially for AFM-based nanoindentation.
- The elastic–plastic properties such as the Young's modulus and yield strength were characterized. We demonstrate the

efficacy of the unloading strain rate principle for improving precision of the AFM nanoindentation measurements of MOF nanosheets.

- Three characteristic failure modes at loading of the nanosheets have been proposed, namely interfacial sliding/slippage (Mode I), framework fracture (Mode II), and delamination (Mode III). The mechanisms are controlled by shear deformation, framework rupture, and bending deformation, respectively. The threshold indentation forces and threshold indentation depths of each of the failure modes have been studied.
- Finite-element modeling has been employed to simulate the AFM nanoindentation of the CuBDC MOF nanosheets to gain insights into the deformation mechanisms underpinning plasticity and failure modes. The model also explains the pop-out and recovery phenomena observed in the nanosheets during the nanoindenter unloading.
- Although the CuBDC nanosheets were chosen in this study as a model material to develop the AFM nanoindentation of metal–organic nanosheets, the general methodologies described are transferrable to probe a wide range of 2-D *van der Waals* layered systems.

6. Author contributions

Z.X.Z. performed the AFM nanoindentation experiments and FEM simulations. I.S.F. synthesized the nanosheet samples and performed the SEM and TEM imaging. Z.X.Z. analyzed the data and prepared the figures under the supervision of J.C.T. Z.X.Z. and J.C.T. wrote the manuscript with input from all authors.

7. Conflicts of interest

The authors declare no competing financial interest.

Acknowledgements

This work was supported by the ERC Consolidator Grant through the grant agreement 771575 (PROMOFS). J. C. T. and I. S. F. thank the EPSRC Grant No. EP/N014960/1 for research funding. The authors acknowledge the Research Complex at Harwell (RCaH) for access to the materials characterization facilities. I.S.F. thanks Dr James Gilchrist for the training and assistance in collecting the TEM images. We are grateful to Dr Gavin Stenning and Dr Marek Jura at R53 Materials Characterization Laboratory (ISIS Rutherford Appleton Laboratory) for providing access to the XRD facilities.

References

1 J. C. Tan and A. K. Cheetham, *Chem. Soc. Rev.*, 2011, **40**, 1059–1080.
2 M. D. Allendorf and V. Stavila, *CrystEngComm*, 2015, **17**, 229–246.
3 A. J. Howarth, Y. Liu, P. Li, Z. Li, T. C. Wang, J. T. Hupp and O. K. Farha, *Nat. Rev. Mater.*, 2016, **1**, 15018.
4 F. Cavallo, D. S. Grierson, K. T. Turner and M. G. Lagally, *ACS Nano*, 2011, **5**, 5400–5407.
5 Z. Jiang, Z. Li, Z. Qin, H. Sun, X. Jiao and D. Chen, *Nanoscale*, 2013, **5**, 11770–11775.
6 F. Cao, M. Zhao, Y. Yu, B. Chen, Y. Huang, J. Yang, X. Cao, Q. Lu, X. Zhang, Z. Zhang, C. Tan and H. Zhang, *J. Am. Chem. Soc.*, 2016, **138**, 6924–6927.
7 M. Chhowalla, H. S. Shin, G. Eda, L. J. Li, K. P. Loh and H. Zhang, *Nat. Chem.*, 2013, **5**, 263.
8 S. Zhao, Y. Wang, J. Dong, C. T. He, H. Yin, P. An, K. Zhao, X. Zhang, C. Gao, L. Zhang, J. Lv, J. Wang, J. Zhang, A. M. Khattak, N. A. Khan, Z. Wei, J. Zhang, S. Liu, H. Zhao and Z. Tang, *Nat. Energy*, 2016, **1**, 16184.
9 A. K. Chaudhari, H. J. Kim, I. Han and J. C. Tan, *Adv. Mater.*, 2017, **29**, 1701463.
10 T. Rodenas, I. Luz, G. Prieto, B. Seoane, H. Miro, A. Corma, F. Kapteijn, F. X. Llabrés i Xamena and J. Gascon, *Nat. Mater.*, 2015, **14**, 48.
11 W. Zhou, H. Wu and T. Yildirim, *Chem. Phys. Lett.*, 2010, **499**, 103–107.
12 E. Hosseini, M. Zakertabrizi, A. H. Korayem and Z. Chang, *J. Chem. Phys.*, 2018, **149**, 114701.
13 K. E. Eshkalak, S. Sadeghzadeh and M. Jalaly, *Comput. Mater. Sci.*, 2018, **149**, 170–181.
14 R. Abadi, R. P. Uma, M. Izadifar and T. Rabczuk, *Comput. Mater. Sci.*, 2017, **131**, 86–99.
15 B. Mortazavi and G. Cuniberti, *RSC Adv.*, 2014, **4**, 19137–19143.
16 R. Ansari, S. Rouhi and S. Ajori, *Superlattices Microstruct.*, 2014, **65**, 64–70.
17 A. Falin, Q. Cai, E. J. G. Santos, D. Scullion, D. Qian, R. Zhang, Z. Yang, S. Huang, K. Watanabe, T. Taniguchi, M. R. Barnett, Y. Chen, R. S. Ruoff and L. H. Li, *Nat. Commun.*, 2017, **8**, 15815.
18 O. V. Penkov, V. E. Pukha, A. Y. Devizenko, H. J. Kim and D. E. Kim, *Nano Lett.*, 2014, **14**, 2536–2540.
19 S. Ozden, Y. Yang, C. S. Tiwary, S. Bhowmick, S. Asif, E. S. Penev, B. I. Yakobson and P. M. Ajayan, *Nano Lett.*, 2016, **16**, 232–236.
20 C. Lee, X. Wei, J. W. Kysar and J. Hone, *Science*, 2008, **321**, 385–388.
21 P. Payamyar, K. Kaja, C. Ruiz-Vargas, A. Stemmer, D. J. Murray, C. J. Johnson, B. T. King, F. Schiffmann, J. VandeVondele, A. Renn, S. Götzinger, P. Ceroni, A. Schütz, L. T. Lee, Z. Zheng, J. Sakamoto and A. D. Schlüter, *Adv. Mater.*, 2014, **26**, 2052–2058.
22 Z. Zeng and J. C. Tan, *ACS Appl. Mater. Interfaces*, 2017, **9**, 39839–39854.
23 Q. Y. Lin, Y. H. Zeng, D. Liu, G. Y. Jing, Z. M. Liao and D. Yu, *ACS Nano*, 2014, **8**, 10246–10251.
24 P. Huang, D. Guo, G. Xie and J. Li, *Nano Lett.*, 2017, **17**, 6280–6286.
25 J. Xu, G. Yuan, Q. Zhu, J. Wang, S. Tang and L. Gao, *ACS Nano*, 2018, **12**, 4529–4535.
26 S. M. Kim, A. Hsu, M. H. Park, S. H. Chae, S. J. Yun, J. S. Lee, D. H. Cho, W. Fang, C. Lee, T. Palacios, M. Dresselhaus,

K. K. Kim, Y. H. Lee and J. Kong, *Nat. Commun.*, 2015, **6**, 8662.

27 D. Kong, W. Megone, K. D. Q. Nguyen, S. Di Cio, M. Ramstedt and J. E. Gautrot, *Nano Lett.*, 2018, **18**, 1946–1951.

28 J. C. Tan, P. J. Saines, E. G. Bithell and A. K. Cheetham, *ACS Nano*, 2012, **6**, 615–621.

29 L. Guo, H. Yan, Q. Moore, M. Buettner, J. Song, L. Li, P. T. Araujo and H. T. Wang, *Nanoscale*, 2015, **7**, 11915–11921.

30 Q. Tu, I. Spanopoulos, E. S. Vasileiadou, X. Li, M. G. Kanatzidis, G. S. Shekhawat and V. P. Dravid, *ACS Appl. Mater. Interfaces*, 2020, **12**, 20440–20447.

31 C. Hermosa, B. R. Horrocks, J. I. Martínez, F. Liscio, J. Gómez-Herrero and F. Zamora, *Chem. Sci.*, 2015, **6**, 2553–2558.

32 D. Jariwala, T. J. Marks and M. C. Hersam, *Nat. Mater.*, 2017, **16**, 170–181.

33 W. Mori, F. Inoue, K. Yoshida, H. Nakayama, S. Takamizawa and M. Kishita, *Chem. Lett.*, 1997, **26**, 1219–1220.

34 J. N. Coleman, M. Lotya, A. O'Neill, S. D. Bergin, P. J. King, U. Khan, K. Young, A. Gaucher, S. De, R. J. Smith, I. V. Shvets, S. K. Arora, G. Stanton, H. Y. Kim, K. Lee, G. T. Kim, G. S. Duesberg, T. Hallam, J. J. Boland, J. J. Wang, J. F. Donegan, J. C. Grunlan, G. Moriarty, A. Shmeliov, R. J. Nicholls, J. M. Perkins, E. M. Grieveson, K. Theuwissen, D. W. McComb, P. D. Nellist and V. Nicolosi, *Science*, 2011, **331**, 568–571.

35 C. G. Carson, K. Hardcastle, J. Schwartz, X. Liu, C. Hoffmann, R. A. Gerhardt and R. Tannenbaum, *Eur. J. Inorg. Chem.*, 2009, **2009**, 2338–2343.

36 S. R. Cohen and E. Kalfon-Cohen, *Beilstein J. Nanotechnol.*, 2013, **4**, 815–833.

37 W. C. Oliver and G. M. Pharr, *J. Mater. Res.*, 2004, **19**, 3–20.

38 A. W. Bowen and P. G. Partridge, *J. Phys. D: Appl. Phys.*, 1974, **7**, 969–978.

39 J. H. Hollomon, *Trans. Metall. Soc. AIME*, 1945, **162**, 268–290.

40 J. R. Matthews, *Acta Metall.*, 1980, **28**, 311–318.

41 M. Bocciarelli, G. Bolzon and G. Maier, *Mech. Mater.*, 2005, **37**, 855–868.

42 Z. Chen, X. Wang, A. Atkinson and N. Brandon, *J. Eur. Ceram. Soc.*, 2016, **36**, 1435–1445.

43 G. R. Johnson and W. H. Cook, *Eng. Fract. Mech.*, 1985, **21**, 31–48.

44 H. Louche, F. Piette-Coudol, R. Arrieux and J. Issartel, *Int. J. Impact Eng.*, 2009, **36**, 847–861.

45 B. Taljat and G. M. Pharr, *Int. J. Solids Struct.*, 2004, **41**, 3891–3904.

46 A. Loganathan, A. Sharma, C. Rudolf, C. Zhang, P. Nautiyal, S. Suwas, B. Boesl and A. Agarwal, *Mater. Sci. Eng., A*, 2017, **708**, 440–450.

47 F. Bédoui, F. Sansoz and N. S. Murthy, *Acta Mater.*, 2008, **56**, 2296–2306.

48 G. M. Pharr, W. C. Oliver and D. S. Harding, *J. Mater. Res.*, 1991, **6**, 1129–1130.

49 E. Garcia, A. Nistal, A. Khalifa, Y. Essa, F. Martín de la Escalera, M. I. Osendi and P. Miranzo, *ACS Appl. Mater. Interfaces*, 2015, **7**, 17656–17662.

50 Y. Chen, S. R. Bakshi and A. Agarwal, *ACS Appl. Mater. Interfaces*, 2009, **1**, 235–238.